PHYSICAL REVIEW RESEARCH **8**, 013231 (2026)

Electrorheoimaging of a nonequilibrium emulsion: Microstructures and multistate switchable viscosities

Majid Bahraminasr[*] and Anand Yethiraj[†]
Department of Physics and Physical Oceanography, Memorial University, St. John's, Newfoundland and Labrador, Canada A1B 3X7
and Department of Physics, University of Guelph, Guelph, Ontario, Canada N1G 2W1

(Received 26 August 2025; accepted 21 January 2026; published 2 March 2026)

Complex fluids such as colloids and emulsions are ubiquitous in biopharmaceuticals, manufacturing, and the oil industry, but controlling their viscosity can pose a significant challenge. Low viscosities are ideal for mixing, high viscosities are helpful for pharmaceuticals, and switchable viscosities are useful for smart materials. One strategy to make multipurpose fluids is to make nonequilibrium modifications to the microstructure of colloids and emulsions using external fields, which can result in emergent changes in their rheological characteristics. We introduce an experimental technique, electrorheoimaging (ERI), which directly visualizes microstructure during rheological measurements while simultaneously applying an electric field. We also introduce a continuous phase that lowers electrohydrodynamic thresholds and enables experiments at modest field strengths, revealing behaviors previously inaccessible in laboratory settings. Using this combination of technique and material design, we observe shear-induced banding that only appears in the presence of electric depending on the frequency of the electric field, at either high or low shear rates. These microstructural transitions produce dramatic, reversible viscosity modulation—not only increases, but also decreases, including negative intrinsic viscosities. Frequency control enables instantaneous switching among multiple effective viscosities spanning a 30-fold range, establishing ERI as a powerful tool for probing and controlling rheology in field-responsive soft materials.

DOI: 10.1103/416j-vpdj

I. INTRODUCTION

The present work focuses on electric-field-responsive emulsions. Electric-field control of droplets is of interest for a range of applications, from microfluidic control [1,2] to coalescence of water drops in crude oil [3,4] to atomization into tiny charged droplets for printing applications [5]. The application of a dc electric field on a single liquid drop dispersed in an immiscible, weakly conducting ("leaky") dielectric liquid leads to steady flows within and around the drop [6–9], with a sensitive dependence on the conductivities, dielectric constants, and viscosities of the two fluids [10,11]. When many drops interact collectively, electrohydrodynamics (EHD) leads to emergent behavior that can be used to make field-responsive oil-in-oil emulsions, which exhibit ordered, disordered, static, or dynamic droplet structures as a function of the amplitude and frequency of an applied electric field [12,13].

While the electrorheological (ER) dipolar response to electrostatic forcing has been examined for decades in particulate suspensions [14–16] and emulsions [17,18], and dynamical forcing has been examined in magnetic fields [19], the electrodynamic effect on rheological response has been much less studied, although early indications of a field-induced reduction in effective viscosities, a "negative ER effect," were likely EHD-related [20]. EHD interactions $[O(a^2/r^2)]$ are longer-ranged than dipolar forces $[O(a^4/r^4)]$, where a is the droplet radius and r is the separation distance between droplet centers. This results in a range of distance-dependent behaviors for pairs of droplets [21,22], with "predator-prey"like dynamics due to nonreciprocal electrohydrodynamic interactions [23]. Electric-field effects on emulsion flow have only been studied to a limited extent experimentally [17,18,24,25], numerically [26], and analytically [27,28].

Combining rheological response with imaging can yield insights into structure-property relations in soft matter [29,30]. This work is admittedly broad in scope. First, we introduce a technique, electrorheoimaging (ERI), that combines electrical forcing, rheological response, and imaging. The ERI setup enables direct, real-time visualization and control of droplet dynamics, and emulsion viscosity under applied electric fields. Second, we present an emulsion system composed of castor oil dispersed in motor oil: Its material parameters are such that we lower the threshold for drop breakup and droplet dynamics behavior, making experiments feasible at high forcing. The above two constitute a methodology. Third, with this methodology, we observe a phenomenon: two kinds of shear-banding instabilities under electric field stimulation, and frequency-controlled and reversible viscosity modification.

---

[*] Contact author: mbahraminasr@mun.ca; m.bahraminasr@uoguelph.ca
[†] Contact author: ayethira@uoguelph.ca

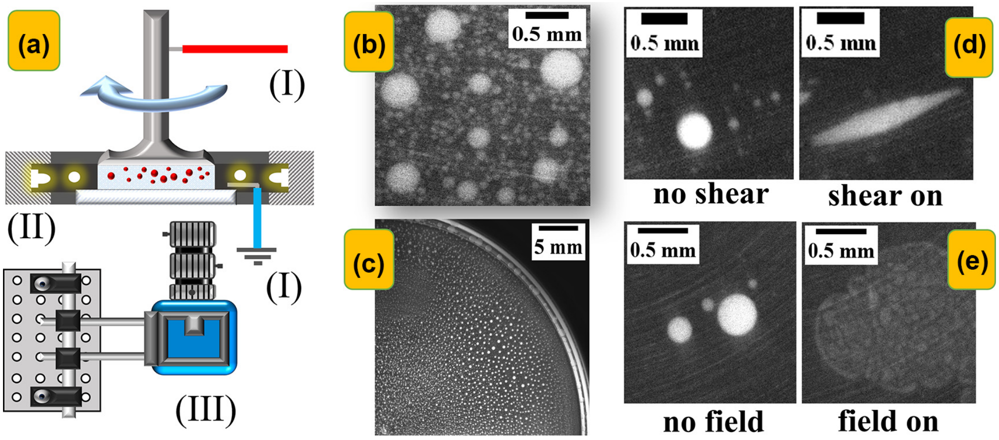

FIG. 1. Schematic and sample images of ERI setup. (a) Electrical contact is made with the high-voltage wire (I, red) attached to the rotating top plate, and the ground wire (I, blue) attached to the fixed bottom plate. The sample is simultaneously illuminated (II) azimuthally from the side. Imaging is performed from the bottom with a camera and macro lens (III) mounted on an axis off-centre with respect to the rheological axis. (b) High magnification: the smallest droplet that can be resolved has a radius of around 30 μm. (c) Low magnification: a magnification that allows imaging an entire quarter-disk region of interest (QD-ROI). (d) Cropped selections of QD-ROI views, at zero electric field, of elongation of droplets along the direction of rotation under no shear (left) and a shear rate of 50 s^{-1} (right). (e) QD-ROI views at $E = 3.7\ \mathrm{V}/\mu\mathrm{m}$: droplets break into smaller droplets, visible as a bright cloud of droplets over a dark background.

II. METHODOLOGY

A. The ERI technique

To directly observe structure-property relationships in emulsions under electric fields, we developed an integrated imaging and rheology platform: ERI. This approach enables simultaneous visualization of microstructure and measurement of rheological properties in real time—providing a direct window into the system's dynamic response.

Figure 1 outlines the ERI setup and demonstrates its spatial resolution and imaging performance. As shown in Fig. 1(a), the system is built around a stress-controlled rotational rheometer (Anton Paar MCR 301). The top plate is a 50-mm diameter stainless steel parallel plate probe, isolated using a Teflon spacer, while the bottom plate is replaced with a transparent, electrically conductive ITO-coated glass disk of the same diameter. Electrical contacts were carefully configured to prevent interference with shear stress measurements (see Sec. VI in the Supplemental Material [31] for details), requiring optimized wiring, as shown in Fig. S1 in the Supplemental Material [31]. A PCO Edge 4.1 camera equipped with a macro lens [item III in Fig. 1(a)] was mounted on a three-axis translation system that was constructed in-house. Section II in the Supplemental Material [31] discusses the illumination in detail. As shown in Fig. S2 in the Supplemental Material [31], the sample was illuminated from the side to minimize reflections off the stainless steel top plate. This approach is akin to dark-field microscopy, e.g., the majority of incident light on the sensor is composed of scattered light from the sample. The dispersed phase was dyed to be darker compared to the suspending medium, resulting in bright droplets on a dark background [Figs. 1(b), 1(d), and 1(e)].

Utilizing this optical setup, the minimum observable droplet radius was approximately 30 μm [Fig. 1(b)]. Collective behaviors were examined globally by imaging a region of interest corresponding to a quarter of a disk, which we refer to as QD-ROI [Fig. 1(c)], which provided a wider view angle at the expense of smaller magnification compared to Fig. 1(b). QD-ROI enables us to connect collective behaviors with rheological signature under simultaneous shear and electric stimulation. In this configuration, the minimum discernible droplet radius was approximately 50 μm, allowing for the observation of elongation of drops in the presence of shear [Fig. 1(d)] as well as fragmentation induced by an electric field, and reorganization into distorted cloudlike structures, in the presence of shear [Fig. 1(e)].

B. An emulsion with low EHD thresholds

To ensure that ERI experiments can be carried out safely and reproducibly across a wide range of electric fields, one needs an emulsion system where the voltage threshold, required to trigger EHD flows, is low. This is a materials challenge. To address this, we formulated an emulsion consisting of castor oil droplets dispersed in motor oil, denoted [Ca:Mo]. Details of the sample materials are given in the Materials section (Appendix). A key advantage of the [Ca:Mo] system is its remarkably low threshold for characteristic EHD phenomena (due to the relatively higher conductivity of the motor oil). Prior work with silicone oil:castor oil ([Si:Ca]) emulsions reported droplet coalescence at approximately 5 V/μm (dc), and breakup at $E \sim 10\ \mathrm{V}/\mu\mathrm{m}$ for drops of radius $a \sim 10\ \mu\mathrm{m}$. In contrast, our microscopy experiments using the cell geometry [Fig. 7(a) in Appendix] reveal that [Ca:Mo] droplets begin to coalesce at just $E = 0.75\ \mathrm{V}/\mu\mathrm{m}$ (dc), as shown in Appendix Fig. 7(b). Droplet breakup follows at a significantly reduced field of $E = 3.6\ \mathrm{V}/\mu\mathrm{m}$ (dc) [see Fig. 7(c) in Appendix].

This dramatic reduction in field thresholds makes ERI tests feasible due to an eight-fold decrease in the electric field intensity E^2 and thus a decrease in propensity for dielectric breakdown, which can damage the stainless steel rheometer plate.

The regime of response of an emulsion can be evaluated by comparing fluid shear, electric dipolar forces, and capillary

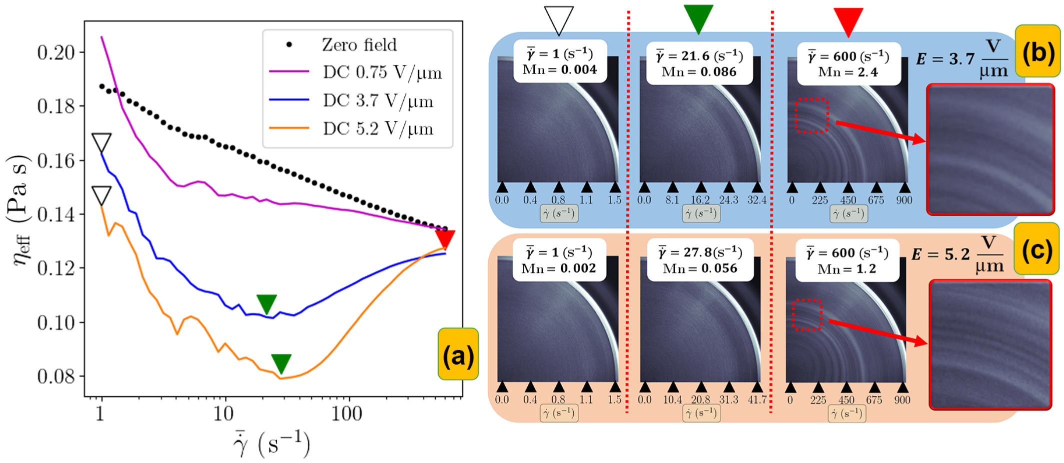

FIG. 2. dc electric fields: viscosity and field-induced banding. (a) At zero field (black dots) ($E = 0$), a modest degree of shear thinning was observed, with η_{eff} decreasing from 0.19 to 0.13 Pa s over the shear rate $\bar{\dot{\gamma}}$ window from 1 to 600 s^{-1}. At $E = 0.75$ V/µm (dc), coalescence-driven layering and accumulation of castor oil on the edge slightly increases η_{eff} at low shear. The application of a dc field with $E = 3.7$ V/µm, blue curve ($E = 5.2$ V/µm, orange curve) results in a qualitative change, i.e., a nonmonotonic dependence of η_{eff} on $\bar{\dot{\gamma}}$: shear thinning from 0 to 21.6 (27.8) s^{-1}, and a noticeable increase in η_{eff} above 21.6 (27.8) s^{-1}. Snapshots at (b) $E = 3.7$ V/µm and (c) $E = 5.2$ V/µm, at $\bar{\dot{\gamma}} = 0$, 21.6, and 600 s^{-1}, show that the onset of banding at and above 21.6 s^{-1} (27.7 s^{-1}) correlates with the shear-rate regime of viscosity increase.

forces. Two useful parameters are the Mason number

$$\mathrm{Mn} = \frac{(3N+2)\eta_2\bar{\dot{\gamma}}}{6(N+1)\kappa_2\epsilon_0\beta^2E^2}, \tag{1}$$

the dimensionless ratio of the viscous and electrical force [26,32], and the electric capillary number

$$\mathrm{Ca_E} = \frac{\kappa_2\epsilon_0\beta^2E^2a}{\gamma_{\mathrm{int}}}, \tag{2}$$

the dimensionless ratio between electric forces and the restoring interfacial tension acting on a drop [26,33]. In the above, N is the viscosity ratio, $\beta = \frac{\kappa_2-\kappa_1}{\kappa_2+2\kappa_1}$ is the Clausius-Mosotti factor, and γ_{int} is the interfacial tension. In our system (parameters in Eq. (A1) in the Materials section of the Appendix), $\mathrm{Ca_E} > 1$ upon initial field application, thus resulting in drop breakup. The Mason number for our system is $\mathrm{Mn} = 0.054\frac{\bar{\dot{\gamma}}}{E^2}$ with the shear rate $\bar{\dot{\gamma}}$ expressed in s^{-1} and E in V/µm. Depending on the $\bar{\dot{\gamma}}$ values, Mn ranges from 0.001 (electrical forces dominate) to above 1 (viscous forces dominate).

III. NEW PHENOMENA

Having established an experimental platform (ERI) and an emulsion system with lower electric field thresholds, in the next section we examine new phenomena in dc and ac electric fields including negative intrinsic viscosities and a frequency-dependent effective viscosity, and culminating in the design of a multistable frequency-controlled viscosity switch.

A. dc fields: viscosity and field-induced banding

Experiments in dc fields reveal striking rheological response, previously unreported: a combination of shear thinning and decreased intrinsic viscosity on one hand, and the emergence field-induced bands in the spatial structure of the sheared emulsion on the other.

Shear thinning and negative intrinsic viscosity: In the absence of an electric field ($E = 0$), the emulsion exhibits shear-thinning behavior, with the effective viscosity η_{eff} [black dots in Fig. 2(a)] decreasing from 0.19 to 0.13 Pa s as the average shear rate $\bar{\dot{\gamma}}$ increases from 1 to 600 s^{-1}. Since the shear rate in a parallel-plate geometry varies radially, we report average values, while local variations in shear rate are illustrated in Figs. 2(b) and 2(c).

In the presence of a modest dc field [$E = 0.75$ V/µm, with conditions identical to those in Fig. 7(b)], EHD flows enhance coalescence of drops, and there is much stronger shear-thinning behavior at low shear rates ($\bar{\dot{\gamma}} < 5$ s^{-1}) followed by more modest shear thinning for $\bar{\dot{\gamma}} = 5$–600 s^{-1}. This is shown in the purple curve in Fig. 2(a). The (dimensionless) intrinsic viscosity for particles in a fluid at volume fraction ϕ [34] measures the effect of particles on the effective viscosity of the medium:

$$[\eta] = (\eta_{\mathrm{eff}}/\eta_2 - 1)/\phi, \tag{3}$$

where, in our system, $\eta_2 = 0.149 \pm 0.002$ Pa s is the motor oil viscosity. The Einstein value for $[\eta]$ is $5/2 = 2.5$, which means that η_{eff} increases by 25% above the medium viscosity when $\phi = 0.1$. We verified that there is indeed a linear dependence of η_{eff} on ϕ [implied by Eq. (3)] for $0.016 < \phi < 0.25$. The intrinsic viscosity can be below the classical Einstein value for dilute emulsions of noninteracting droplets [27]. For the quiescent [Ca:Mo] emulsion (i.e., zero electric field and in the zero-shear limit), at a castor oil droplet volume fraction $\phi = 0.091$, $\eta_{\mathrm{eff}} \equiv \eta_0 = 0.19$ Pa s. Using the motor oil viscosity $\eta_2 = 0.149 \pm 0.002$ Pa s, we obtain an intrinsic viscosity $[\eta] = 3.0$, which is higher (not lower) than the Einstein value. As the field E is increased, η_{eff} at $\bar{\dot{\gamma}} = 1$ s^{-1} decreases and at $E = 5.2$ V/µm, it is below the value of η_2, i.e., *the intrinsic viscosity* $[\eta]$ *is negative*.

For stronger dc fields of $E = 3.7$ and 5.2 V/µm (blue and orange curves, respectively, in Fig. 2(a), respectively), there is a minimum in η_{eff} at $\bar{\dot{\gamma}} = 20$–30 s^{-1} (indicated by inverted green triangles). Notably, for modest $\bar{\dot{\gamma}}$ at $E = 5.2$ V/μm (dc), η_{eff} is well below that of the zero-field emulsion, i.e., $\eta_{\text{eff}} < \eta_2$ and $[\eta] < 0$. On the other hand, at very low shear rates and at $E = 0.75$ V/μm, field-induced coalescence creates castor-oil-rich layers at the electrodes, slightly elevating η_{eff} by effectively reducing the motor-oil gap. A small additional increase may come from castor oil collecting near the plate edges. These artifacts disappear at higher fields, where EHD-driven breakup prevents segregation and the emulsion remains homogeneous.

Banding. Figures 2(b) and 2(c) show QD-ROI images at dc fields $E = 3.7$ and 5.2 V/μm, and at low (inverted black triangles, $\bar{\dot{\gamma}} = 1\,\text{s}^{-1}$), intermediate (inverted green triangles, $\sim 20\,\text{s}^{-1}$), and high (inverted red triangles, $\bar{\dot{\gamma}} = 600\,\text{s}^{-1}$) shear rates. At intermediate $\bar{\dot{\gamma}}$, we see the emergence of sharp variations in image brightness (bright and dark bands that arise from light scattering in the presence of droplet density variations) as a function of radial distance from the center in Figs. 2(b) and 2(c): These bands are highlighted in the insets of small ROIs shown on the right of the figures. In the breakup regime (3.7 V/μm and above), there is a strong correlation, over several replicates of each experiment, between an increase in viscosity and band formation. Movie 1 in the Supplemental Material [31] illustrates the emergence of banding during a shear-rate ramp from 21.6 to 600 s^{-1} at $E = 3.7$ V/μm dc [corresponding to the blue curve in Fig. 2(a)].

A small subset of these results have been previously observed, for example, in a computational study [26], carried out for an emulsion in a dc electric field with $\text{Ca}_\text{E} \ll 1$, which exhibited strong, monotonic shear-thinning behavior due to the formation of droplet chains (also referred to in the literature as columns) at low Mn. This result is consistent with our observations at low Ca_E and Mn. However in our experiment, we also access the drop breakup regime, where η_{eff} first decreases at low $\bar{\dot{\gamma}}$, but then increases unexpectedly at higher $\bar{\dot{\gamma}}$. Possible mechanisms for this phenomenon, coupled with the diffuse banding observed at high shear rates in the EHD regime, are addressed in Sec. IV.

B. ac fields: nonmonotonic frequency-dependent viscosity and microstructure regimes

Electrohydrodynamics is strongly frequency dependent. The Clausius-Mosotti factor [35] β in the dipolar force ($F_{\text{dipolar}} \sim \beta^2 E^2$) [26] is roughly frequency independent in the range of our experiments (dc, 500 Hz), while EHD gets weaker with increasing frequency so that the interactions should cross over from EHD-dominated to dipolar-dominated with increasing frequency. In the framework of leaky-dielectric EHD [7,10], the onset of EHD flow depends on material property ratios between the dispersed (inner) and continuous (outer) phases: conductivity $H = \sigma_{E,1}/\sigma_{E,2}$, permittivity $S = \kappa_1/\kappa_2$, and viscosity $N = \eta_1/\eta_2$. Under ac stimulation, there is a transition between oblate drop deformation (in the low-frequency EHD regime) and prolate drop deformation above a critical frequency f_c, which is a function of H, S, and N [10]; this critical frequency exists when $\frac{S}{H} \geqslant 1 + (5H(1+N)(1/H-1)^2)/(16+19N)$.

We investigated the frequency response of the emulsion via microscopy and ERI experiments between 0 and 500 Hz. Each experiment was performed in a 270 μm cell using the [Ca:Mo] emulsion at a fixed volume ratio of 1:10. Sinusoidal ac fields with an rms amplitude of $E_{\text{rms}} = 3.7$ V/μm were applied at 18 distinct frequencies ranging from 0.25 to 500 Hz. For comparison, each run also included control measurements under dc fields with $E = 3.7$ V/μm as well as for $E = 0$.

These experiments revealed three distinct frequency regimes, each marked by characteristic flow behaviors and structural responses, with largely reversible transitions between them. In regime I ($f < 10$ Hz), strong EHD flows lead to negative intrinsic viscosity and enhanced shear thinning. At high frequencies (regime III, $f > 60$ Hz), EHD forces are much weaker than the field-induced dipolar forces, which lead to the formation of droplet chains aligned along the field direction, accompanied by an apparent yield stress and a pronounced increase in viscosity. Regime II is a transitional regime at intermediate frequencies (10–30 Hz) where EHD flows are strong enough to generate weak flows that increase droplet coalescence.

Figure 3(a) shows the behavior of η_{eff} as a function of $\bar{\dot{\gamma}}$ in ac fields, for a few landmark frequencies at 2 Hz (regime I), 10 and 30 Hz (regime II), and 60 and 500 Hz (regime III). Shown for comparison is the effective viscosity at zero field, which shows a modest degree of shear thinning as a function of $\bar{\dot{\gamma}}$. It should be noted that this arises from a shear stress σ versus $\bar{\dot{\gamma}}$ that is nearly linear, i.e., showing nearly Newtonian behavior (the dotted line with a slope close to 1 on the log-log plot in Fig. S3 in the Supplemental Material [31]).

In Fig. 3(b), η_{eff} at a low shear rate $\bar{\dot{\gamma}} \sim 1\,\text{s}^{-1}$ (and $E_{\text{rms}} = 3.7$ V/μm) is plotted as a function of frequency: η_{eff} decreases from 0.19 Pa s at zero field to 0.03 Pa s at 2 Hz (a factor of 6 reduction). This is the "negative ER regime" referred to in the electrorheology literature [20], and EHD is the likely cause. The intrinsic viscosity [shown on the right axis in Fig. 3(b)] is strongly negative, reaching a value as low as $[\eta] = -9.25$. In regime I, EHD forces are dominant and η_{eff} is much lower than the quiescent (zero electric field) viscosity $\eta_0 = 0.19$ Pa s [Fig. 3(b)]. This regime (low-frequency ac) thus shows trends that are very similar to those for dc fields, with shear thickening past a threshold $\bar{\dot{\gamma}}$ [Fig. 3(a), plots at several frequencies between 10 mHz and 2 Hz are shown in Fig. S4 in the Supplemental Material [31]]. We see in Fig. 3(b) that between 10 and 30 Hz (regime II), η_{eff}/η_0 increases back to 0.84 and $[\eta]$ [defined in Eq. (3)] goes back to zero. This is the frequency crossover from EHD- to dipolar-dominated. The rheological behavior [i.e., η_{eff} versus $\bar{\dot{\gamma}}$ flow curve in Fig. 3(a)] is between that for dc and that for zero field. Beyond 30 Hz (regime III), η_{eff} increases sharply to a maximum value of 1 Pa s at 500 Hz, i.e., $\eta_{\text{eff}} \sim 5.3\eta_0$ and is a factor of 30 higher than the value at 2 Hz. In regime III, the system develops a yield stress, as shown in Fig. S3 in the Supplemental Material [31]. This results in an effective viscosity that starts high but decreases, $\eta_{\text{eff}} \sim \eta + \sigma_0/\bar{\dot{\gamma}}$, so a yield stress $\sigma_0 = 1$ Pa contributes 1 Pa s to η_{eff} at $\bar{\dot{\gamma}} = 1\,\text{s}^{-1}$. The large calculated value of $[\eta] \sim 57$ is reflective of the fact that percolating droplet dipolar chains, even at low ϕ, have an outsize effect on effective emulsion viscosity (it is these percolating chains that result in a yield stress).

Figures 3(c)–3(g) show microscopy images of droplets at zero field and at $E_{\text{rms}} = 3.7$ V/μm in regime I (2 Hz), II

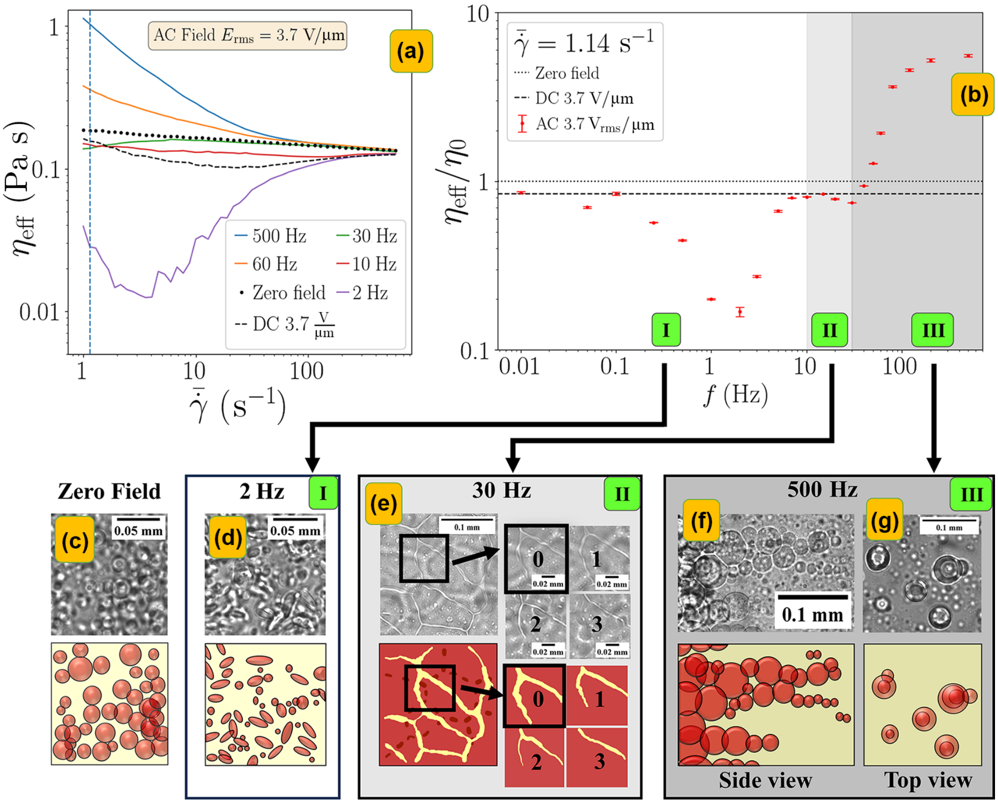

FIG. 3. ac fields: nonmonotonic frequency-dependent viscosity and microstructure regimes. (a) The apparent viscosity $\eta_{\mathrm{eff}} = \sigma/\bar{\dot{\gamma}}$ highlights the salient features: nearly Newtonian (very modestly shear thinning) behavior at zero field, high-frequency (500–60 Hz) shear thinning that is classic yield-stress behavior, while at lower frequencies, shear thinning at $\bar{\dot{\gamma}} < 10\,\mathrm{s}^{-1}$ is followed by an increase in η_{eff}. (b) η_{eff} ($\bar{\dot{\gamma}} \sim 1\,\mathrm{s}^{-1}$), indicated with a vertical, blue dashed line in panel (f) shows a modest decrease in a dc field from the zero-field value $\eta_0 = 0.19$ Pa s. $\eta_{\mathrm{eff}}/\eta_0$ shows a pronounced decrease at low (ac) frequencies (region I, <10 Hz). Between 10 and 30 Hz (region II), η_{eff} is nearly identical to the dc field value. At higher frequencies (regime III), there is substantial *increase* in η_{eff}. (c)–(g) Micrographs at different frequencies (top) with sketches (bottom) indicating castor oil (red) and motor oil (yellow). (c) Zero field: spherical castor oil droplets with sizes ranging from ~10 to 30 μm. (d) 2 Hz, $E_{\mathrm{rms}} = 3.7$ V/μm, regime I: droplets undergo continuous breakup along with coalescence with average sized smaller than zero field. (e) 30 Hz, $E_{\mathrm{rms}} = 3.7$ V/μm, regime II: droplets gather on each electrode, making it the sample transparent. Given sufficient time, the packed droplets merge, forming a sheet of castor oil on each electrode (labeled 0–3). (f), (g) 500 Hz, $E_{\mathrm{rms}} = 3.7$ V/μm, regime III: droplets exhibit prolate deformations and form chain structures [shown in side view (f) and top views (g)].

(30 Hz), and III (500 Hz). At zero field [Fig. 3(c)], the system is completely static in the absence of shear. In regime I, and in the absence of shear, the system is in a dynamic steady state, with a balance of drop deformation, breakup, and coalescence [Fig. 3(d), 2 Hz], much as it is in dc fields. In regime II (30 Hz), droplets grow larger through coalescence and can collect near the electrodes. The packing of castor oil droplets becomes stronger, with nearly all droplets on one side of the electrode and the pattern on the other electrode becoming visible [Fig. 3(e)]. Between 30 and 130 Hz, drop deformations are oblate (signifying importance of EHD) but drops begin to form chains, indicating the increasing importance of dipolar forces with increasing frequency.

At 500 Hz (regime III), droplets are pinned to their location and form chains of droplets [Figs. 3(f) and 3(g) show the side view and top view].

C. A multistable viscosity switch

A key outcome of these observations is the demonstration of a fast, reversible viscosity switch, achieved simply by tuning the frequency of the applied electric field. This switchable control over the fluid's rheological state offers potential for adaptive and programmable materials.

Figure 4 illustrates the ability to toggle between distinct flow states: switching from 2 to 500 Hz causes the apparent viscosity η_{eff} to increase from approximately 0.03 to 1 Pa s. This switching is reversible. These changes occur within seconds, as confirmed by time-resolved imaging of structure formation and breakup. The reversibility of this process is highlighted in Fig. 4(a), which shows η_{eff} during a continuous shear rate ramp. The ac field was initially applied at $E_{\mathrm{rms}} = 3.7$ V/μm and 2 Hz, with shear beginning at low $\bar{\dot{\gamma}}$. Near $\bar{\dot{\gamma}} = 10\,\mathrm{s}^{-1}$, the field was turned off, and later reapplied at 100 Hz when the $\bar{\dot{\gamma}} \sim 100\,\mathrm{s}^{-1}$. The viscosity curve closely retraces the behavior from separate experiments conducted at 2 and 100 Hz, demonstrating the robustness and repeatability of the switching mechanism.

What is remarkable about the system is that this behavior can be switched on and off at will between *multiple states* at different viscosities. Figure 4(b) shows an experiment where the shear rate was maintained at $\bar{\dot{\gamma}} = 1\,\mathrm{s}^{-1}$. At $t \sim 100$ s, the

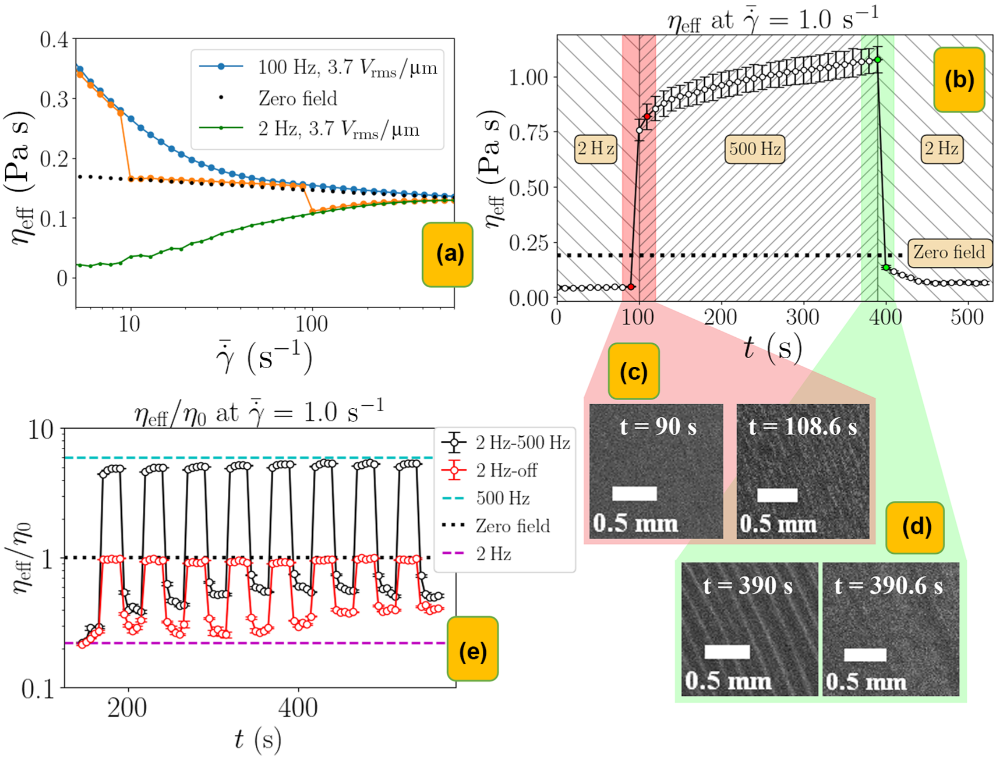

FIG. 4. A multistable viscosity switch: Changing the frequency can cause sudden and reversible changes. (a) Apparent viscosity η_{eff} vs $\bar{\dot{\gamma}}$ shows that switching the field from 100 to off to 2 Hz yellow line [matches the curves of 100 Hz (blue line), zero field (black dotted line), and 2 Hz (green line)]. (b)–(d) Formation and destruction of bands: (b) At a fixed $\bar{\dot{\gamma}} = 1$ s^{-1}, η_{eff} changes drastically when switching from 2 to 500 Hz and vice versa. (c) Changing f from 2 to 500 Hz it takes several seconds for bands to become clearly visible at $\bar{\dot{\gamma}} = 1$ s^{-1}. (d) When switching back from 500 to 2 Hz, bands are destroyed almost instantly. (e) η_{eff} changes periodically with field changes from 0 to 2 Hz (red circles) and 2 to 500 Hz (black circles), compared to values from experiments at $\bar{\dot{\gamma}} = 1$ s^{-1} for 500 Hz (dashed cyan), zero field (black dotted), and 2 Hz (dashed magenta).

frequency was switched between 2 and 500 Hz, which are the two frequencies that show the maximum η_{eff} difference at $\bar{\dot{\gamma}}$. The frequency was switched back to 2 Hz around $t \sim 400$ s. It should be noted that there is a modest increase in η_{eff} between 100 and 400 s, which also corresponds to a refinement of the bands, comparing the micrographs shown at $t = 108.6$ s and $t = 390$ s in Figs. 4(c) and 4(d), respectively. Figure 4(e) shows that repeated switching causes a modest change in the value of η_{eff} at 500 Hz, no change in the field-off characteristics, and a modest increase in the value of η_{eff} at 2 Hz (which looks more appreciable because of the logarithmic scale). This is a three-state switch between $\eta_{\text{eff}} = 0.04$, 0.2, and 1 Pa s: many more states are of course possible. This ability to modulate viscosity in real time through external fields opens avenues for designing responsive materials with on-demand mechanical properties.

IV. DISCUSSION

We have devised a methodology, ERI, which allows us to combine quantitative macroscopic rheological measurements in the presence of an electric field with qualitative insights from optical imaging. This is useful because connecting ER properties to microscopic behavior is challenging. Imaging a QD-ROI also enables the detection of bubbles, which can seriously affect rheological measurements.

In the absence of EHD forces, anisotropic dipolar interactions result in the formation of chainlike structures aligned along the electric field; these configurations are well established in low-shear colloidal and emulsion systems [36]. The ERI study reveals two qualitatively distinct shear banding modes, arising from different underlying mechanisms, as shown in the f–$\dot{\gamma}$-phase diagram [Fig. 5(a)]. Dipolar banding [Fig. 4(d)] occurs in regime III (at high frequencies) and low average shear rates. In contrast, EHD banding [Figs. 2(b) and 2(c)] emerges at very low ac frequencies (regime I) or under dc fields, and only at sufficiently high $\bar{\dot{\gamma}}$. Dipolar bands are sharp while EHD bands are spatially diffuse structures. The solid line in Fig. 5(a) represents the boundary of the dipolar region, determined by the appearance of bands at lower shear rates. Reducing frequency does not weaken dipolar forces but enhances EHD, which supply additional charges and reinforce the chains as long as dipolar forces remain dominant over EHD. Lowering the frequency, one first observes a regime with no banding, which we refer to as “no-band land.” This no-band land includes regime II and the region of regime I with the lowest η_{eff} (roughly from 30 to 0.1 Hz). At lower frequencies ($f < 0.1$ Hz), EHD-induced diffuse banding is observed as in dc.

Dipolar banding. In regime III, droplets organize into well-defined, chainlike structures aligned along the vorticity direction. Dipolar banding is observed at relatively low

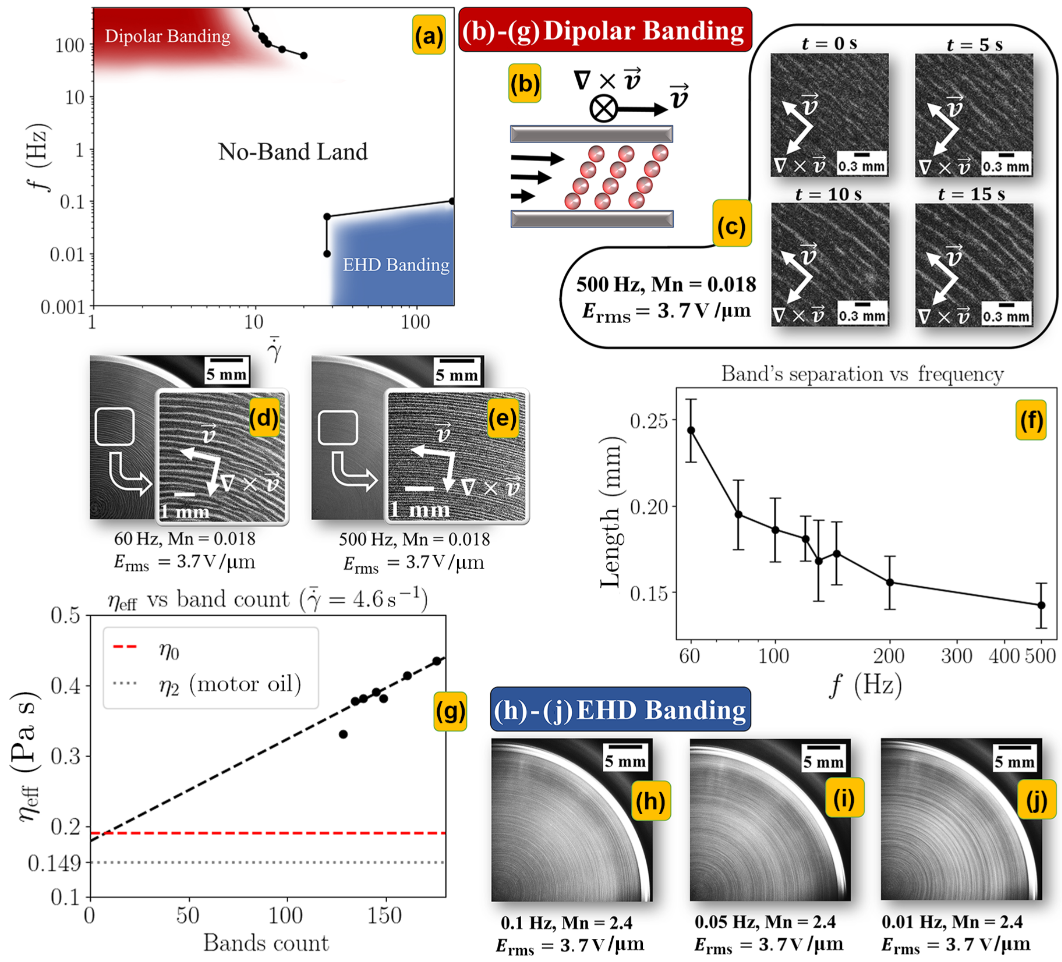

FIG. 5. Two kinds of shear banding: (a) f–$\dot{\gamma}$-phase diagram (at $E_{\rm rms} = 3.7\,{\rm V}/\mu{\rm m}$) illustrates two distinct types of banding: in the dipolar regime (regime III) at low $\bar{\dot{\gamma}}$, and in the EHD regime (regime I) at very low ac frequencies but high $\bar{\dot{\gamma}}$. (b)–(g) Dipolar banding. (b) Chain formation in ac: At high frequencies, dipolar forces are stronger than hydrodynamics, causing droplets to form chains. Shear spreads these chains along the direction of flow. (c) Over time, they form arches and eventually rings. (d), (e) Banding in regime I ($\bar{\dot{\gamma}} = 4.6\,{\rm s}^{-1}$, 500 and 60 Hz), $E_{\rm rms} = 3.7\,{\rm V}/\mu{\rm m}$. (f) Band separation decreases with frequency in regime III. (g) $\eta_{\rm eff}$ (at $\bar{\dot{\gamma}} \sim 4.6\,{\rm s}^{-1}$) decreases with decreasing number of bands; a linear extrapolation to zero yields a viscosity that is very close to η_0 (the quiescent emulsion viscosity). (h)–(j) EHD banding. EHD banding at low f is identical in nature to EHD banding in dc fields. (h)$f = 0.1$ Hz. The first sign of banding appears near the edge of the disk at $\bar{\dot{\gamma}} = 167\,{\rm s}^{-1}$. Bands are more pronounced as frequency is reduced, (i) to $f = 0.05$ Hz and (j) to $f = 0.01$ Hz. At $f = 0.05$ and $f = 1$ Hz, band formation occurs at $\bar{\dot{\gamma}} = 27.8\,{\rm s}^{-1}$, as in dc.

Mason numbers (Mn ~ 0.02). At high frequencies, dipolar forces dominate over EHD forces, leading to the formation of droplet chains [Fig. 5(b)]. Under shear, these chains elongate in the flow direction $\vec{v}$ with dipolar attractions collecting them into bands that are spaced roughly equally in the vorticity direction $\nabla \times \vec{v}$ [Fig. 5(c)]. Banding (also called "lamella formation") has been seen to occur in dipolar colloidal suspensions [37,38]. It was shown in Ref. [37] that concentration fluctuations, which lead to dielectric constant fluctuations in space, affect the electrostatic free energy anisotropically: Only fluctuations parallel to the vorticity direction are unaffected by shear and continue to grow, giving rise to stable concentration variations in the vorticity direction, i.e., banding. Increasing shear destroys these dipolar bands; thus, dipolar bands are only observed at low $\bar{\dot{\gamma}}$.

Figures 5(d) and 5(e) show dipolar banding at 500 and 60 Hz, respectively, both at a shear rate of ~4.6 s^{-1}. The bands at 60 Hz exhibit larger separation and width. The emergence of these bands correlates with the viscosity increase observed in regime III, as regions of high and low density repeatedly form. Movie 2 in the Supplemental Material [31] illustrates banding at $f = 100$ Hz and at low $\bar{\dot{\gamma}}$. The band separation depends on frequency [Fig. 5(f), at $\dot{\gamma} = 4.6\,{\rm s}^{-1}$]. To calculate the spacing of the bands, image intensity variations were analyzed using ImageJ along a line perpendicular to the bands: local maxima determined band locations. Figure 5(g) shows that the measured $\eta_{\rm eff}$ is directly related to the number of bands in the sample: increasing the number of bands increases the effective viscosity in a linear fashion; the intercept corresponding to zero bands has a value of 0.18 Pa s. This, interestingly, is close to the the quiescent, zero-field value of the emulsion viscosity $\eta_0 = 0.19$ Pa s.

EHD banding. EHD banding requires stronger forcing than dipolar banding, with Mn > 0.05 and often exceeding unity. In both cases, banding emerges when the electric Capillary number Ca$_{\rm E}$ approaches unity, highlighting the critical

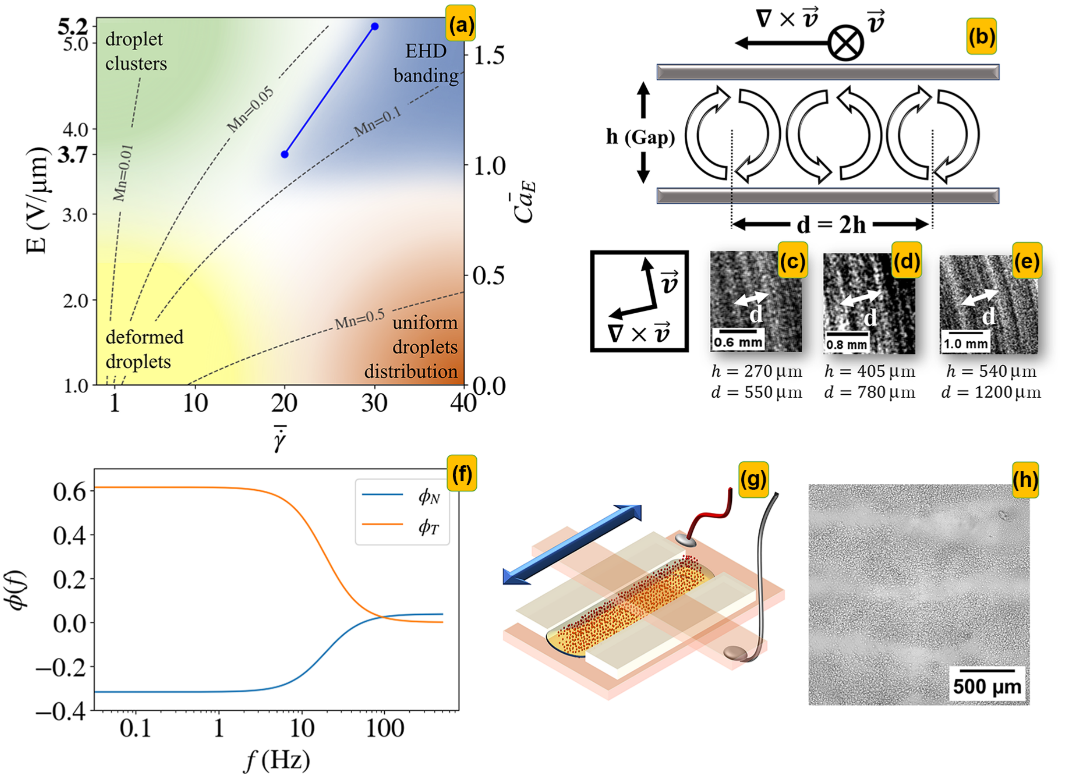

FIG. 6. Mechanism for EHD banding. (a) Phase diagram of field strength vs average shear rate in dc fields. At low electric fields (below the breakup threshold) and low shear rates, droplets deform without breaking. As the shear rate increases while the electric field remains constant, larger droplets begin to break up. The blue line that connects the two experiments at $E = 3.7$ and $5.2\,\mathrm{V}/\mu\mathrm{m}$ (dc) indicates the values of $(E, \bar{\dot{\gamma}})$ for the onset of EHD banding. (b) Convection rolls (view parallel to the flow direction): The distance between two convection rolls separated by one intermediate band (i.e., every other band) is twice the gap thickness, denoted as d. (c) For gap $h = 270\,\mu\mathrm{m}$, $d = 550\,\mu\mathrm{m}$. (d) For $h = 405\,\mu\mathrm{m}$, $d = 780\,\mu\mathrm{m}$. (e) For $h = 540\,\mu\mathrm{m}$, $d = 1200\,\mu\mathrm{m}$. In panels (c)–(e), $d/h = 2.06 \pm 0.15 \approx 2$. (f) Frequency dependence of EHD forces: Dimensionless stress components ϕ_T (tangential) and ϕ_N (normal) display the variation of the EHD forces with frequency for the material parameters in our experimental system. (g) Linear parallel plate experiment setup consisting of two ITO-coated plates, separated by 250 μm. The top plate is unglued and can move freely back and forth. (h) Flow-aligned banding: In the presence of both shear and electric field, bands with thickness comparable to the cell gap are created.

balance between electric stresses and interfacial tension. EHD flows can either enhance or oppose the effects of dipolar chaining [21,22,39,40] depending on the frequency and fluid properties. At sufficiently strong EHD activity, the convective flows disrupt chain formation entirely, as also seen previously [18], but we only observe banding under dc or low-frequency ac stimulation. At 2 Hz in regime I, the rheological signature begins to resemble dc behavior [Fig. 3(a)] but without exhibiting periodic structures (Movie 3 in the Supplemental Material [31], 2 Hz). At frequencies below 0.1 Hz, signs of EHD banding appear near the edges [Fig. 5(h)]. The bands are more pronounced at 0.05 Hz [Fig. 5(i)] and even more so at 0.01 Hz [Fig. 5(j) and Movie 4 in the Supplemental Material [31]]. While the dipolar banding observed at high frequencies is readily attributed to a competition between shear and field-induced dipole-dipole interactions, the origin of the EHD banding seen at low frequencies or under dc fields requires closer examination.

Mechanism for EHD banding: Shear banding is generally classified into three categories [41–43]: (1) gradient banding, involving variations in viscosity along the velocity gradient direction; (2) vorticity banding, where bands of different stress alternate along the vorticity direction but are aligned in the flow direction; and (3) vorticity-aligned banding, characterized by log-rolling structures aligned with the vorticity and alternating along the flow direction. In emulsions, such vorticity-structured states have been previously reported, including both vorticity banding [44,45] and vorticity-aligned banding [43]. In colloidal systems, similar patterns have been linked to attractive interactions between particles [46–52]. Collectively, these studies indicate that the type of banding observed is strongly influenced by the balance between flow-induced forces and internal cohesive forces. A numerical study [53] based on the rheology of emulsions [44,45] has reinforced the role of coalescence in maintaining the stability of banded structures. Both the dipolar and EHD banding modes manifest as alternating bands oriented perpendicular to the vorticity and along the flow direction, i.e., vorticity banding.

An E–$\bar{\dot{\gamma}}$-phase diagram [Fig. 6(a)] is shown for dc fields. At low shear rate and low field strength ($\mathrm{Mn} < 1$, $\mathrm{Ca_E} < 1$), there are stable deformed drops. For higher Mason number $\mathrm{Mn} > 0.5$ (but $\mathrm{Ca_E} < 1$) shear breaks up deformed drops into a relatively uniform distribution of droplet sizes. Field-induced droplet breakup occurs when $\mathrm{Ca_E} > 1$: EHD banding only occurs above the threshold for droplet breakup

($\mathrm{Ca_E} > 1$) and for high Mason number ($\mathrm{Mn} > 0.05$), confirming this balance of breakup, coalescence, and shear.

In the current work (and also observed previously [54]), EHD-induced electroconvection (Fig. S5 in the Supplemental Material [31] shows drops going in and out of focus in two snapshots 70 ms apart) gives rise to cloudlike structures on the scale of the cell's thickness [Fig. 6(b)]. ERI experiments at different gap separations h [Figs. 6(c)–6(e)] exhibited band spacings *at onset* that were comparable with twice the gap separation d: $d \approx 2h$. Moreover, the temporal frequency of convection rolls ($\sim$1 Hz) is remarkably close to the frequency (2 Hz) of the viscosity minimum. EHD forces have an expected frequency dependence that matches our observations. Figure 6(f) shows dimensionless EHD stress components, ϕ_T (tangential) and ϕ_N (normal) [10] (see Sec. V in the Supplemental Material [31] for more details): Their magnitude rises from a value close to zero at high frequency to their maximum value (order unity) as the frequency is reduced to 1 Hz and below.

The above observations help narrow down the cause of EHD banding: it emerges out of a competition between EHD convection (observed in the absence of shear at low frequency) and shear flow. To examine whether shear rate gradients (present in our rotary-shear system) influence EHD shear banding, a linear-shear parallel-plate shear cell was constructed, in which the top plate was allowed to move back and forth freely [Fig. 6(g)]: This setup avoids the $\dot{\gamma}$ gradients of rotational rheometry, but maintains the gap spacing and the dc field strength. The top plate was moved at a speed of approximately 3 cm/s. Under these conditions, we consistently observed bands aligned with the flow direction [Fig. 6(h)], with spacing and thickness comparable to the cell gap. Here, too, the banded structure only appeared in the presence of both an electric field and shear. We find that banding occurs in the higher viscosity regions, effectively a system's response that limits viscosity increases.

Despite the dissipative nature of EHD flows, our system displays remarkably reproducible phase behavior and reversible transitions between distinct flow states. The nonequilibrium phase diagrams, such as those in Figs. 5(a) and 6(a) represent transitions into nonequilibrium steady states (NESSes), in which a dynamic balance is maintained between droplet breakup, coalescence, and hydrodynamic interactions.

Connection between morphology and viscosity changes: The two banding modes provide a direct link between morphology at the QD-ROI scale and the measured flow curves. In the dipolar regime, densely packed, field-aligned chains resist deformation and give rise to a finite yield stress and a strong increase of η_{eff} at low $\bar{\dot{\gamma}}$. We believe that banding is a system's response to this: the collection of these chains into azimuthal bands of droplets at discrete radial distances limits the viscosity increase. In the EHD regime, diffuse bands associated with convection rolls appear precisely in the shear-rate range where the dc and low-frequency flow curves turn back upward, showing that the formation of these large-scale structures correlates with the nonmonotonic rheological response.

V. CONCLUSION

For dc and low-frequency ac fields (below 2 Hz) η_{eff} has a minimum at low shear rates. We link this behavior to electroconvection observed during droplet breakup, with convection rolls occurring at a characteristic frequency of around 1 Hz (see Fig. S5 and Sec. V in the Supplemental Material [31]). At ultralow frequencies ($0 \leqslant f < 0.1$ Hz) and in dc fields, EHD banding is observed in the presence of shear when electrical forcing is at frequencies much smaller than the temporal frequency of convection rolls.

At intermediate ac frequencies, the viscous response is roughly in between that of zero field and a dc field. In this regime (regime II, $10 < f < 30$ Hz, $E_{\mathrm{rms}} = 3.7\,\mathrm{V}/\mu\mathrm{m}$), droplets exhibit oblate deformation, and the micrographs indicate that the droplet phase flattens and segregates toward the electrodes leaving the bulk (motor oil) fluid in the center, which explains the observed viscous response.

While orders-of-magnitude changes in viscosity can be achieved, for example, at a phase transition, the ability to achieve viscosity change that is controlled by frequency, not by field strength, and does not require a phase transition, makes the applicability of this phenomenon much broader. At high ac frequencies (regime III, $f > 60$ Hz, $E_{\mathrm{rms}} = 3.7\,\mathrm{V}/\mu\mathrm{m}$), there is a marked increase in the apparent viscosity at low shear rates, due to the emergence of a yield stress. This is classic ER behavior with a difference: in classic ER behavior there are solid particles in a fluid; in this case, there is a two-fluid medium with no particulates. This ER response is therefore not as pronounced as one with particles; the use of particles as additives would likely enhance this response. Nevertheless, an increase in the apparent viscosity correlates with a banding instability driven by both electric fields and shear fields, with the band separation decreasing with increasing ac frequency. Unlike dc fields, where banding is seen at moderate shear rates, the banding here is strongest at low shear rates. Moreover, the banding here is more regular in spacing. The apparent viscosity increases inversely with the band spacing and linearly with the number of bands. These bands are composed of inner-phase fluid that would be extended along the field direction in the absence of shear, but gets smeared into the shear direction in the presence of shear; however, this need to overcome dipolar forces enhances the apparent viscosity at high frequencies, in comparison with zero field.

Unlike systems exhibiting either a standard ER effect [14,55–58] or the giant electrorheological (GER) effect [59–61], our system can also reduce viscosity below the quiescent, field-off state. Toggling frequency instead of field amplitude simplifies control. Notably, combining this approach with suitable particles could enhance the effect by integrating polarization mechanisms from ER or GER with EHD interactions. The realization of a multistate viscosity switch that is frequency controlled is potentially useful in applications for stimuli-responsive materials and materials with field-configurable mechanical properties.

While the measurements reported have been carried out for a droplet-phase volume fraction $\phi = 0.09$, both viscosity enhancement (at high ac frequencies, $f = 500$ Hz) and viscosity reduction (at low frequencies and dc) is observed at a range of

ϕ from 0.016 to 0.25, indicating that multistable switchability of the viscosity is thus fairly robust.

A unifying framework for understanding nonequilibrium systems—such as living matter—remains an open challenge in physics [62]. Beyond its relevance for designing smart, responsive materials [63], our ERI methodology provides a platform for the study of energy dissipation, pattern formation, and nonequilibrium steady states in driven fluids; it not only provides a direct link between electrorheological response and microstructure but also helps detect artifacts, such as bubbles, that could distort measurements. Furthermore, the ERI technique is applicable more widely in soft materials beyond the current emulsion system, and can also be used to study ER mechanisms in particulate systems.

ACKNOWLEDGMENTS

The authors acknowledge the support of the National Science and Engineering Research Council of Canada (No. RGPIN-2019-04970 and No. RGPIN-2025-05494). This research was undertaken, in part, thanks to funding from the Canada Research Chairs Program. All design and construction were completed in-house, with extensive support from the Memorial University Physical Sciences Machine Shop.

DATA AVAILABILITY

The data that support the findings of this article are not publicly available. The data are available from the authors upon reasonable request.

APPENDIX

1. Materials

In this experiment, we used an emulsion of castor oil in motor oil, specifically NOW Solutions castor oil and Irving MAX1 10W-30 motor oil. The electrical conductivity (σ_E) of castor oil (motor oil) was measured at 3.96 ± 0.01 picomho/cm (102 ± 1 picomho/cm), the relative permittivity (κ) at 5.9 ± 1.3 (2.58 ± 0.52), and the viscosity (η) at 0.961 ± 0.002 Pa s (0.149 ± 0.002 Pa s), respectively. A similar experiment with silicone oil showed a conductivity of 0.33 ± 0.01 picomho/cm, a relative permittivity of 2.6 ± 0.1 and a viscosity of 0.150 ± 0.001 Pa s. The inner-to-outer dielectric constant ratio, conductivity ratio, and viscosity ratio:

$$S = 1.32, \quad H = 0.04, \quad N = 6.45. \tag{A1}$$

Emulsions consisting of at least one leaky dielectric that satisfy the condition $S/H \geqslant 1 + \frac{5H(1+N)(1/H-1)^2}{16+19N}$, have been shown [10] to exhibit a characteristic electrical field frequency below which droplets deformations are oblate (the regime dominated by electrohydrodynamic forces) and above which the deformations are prolate (the regime dominated by dipolar forces). In the [Ca:Mo] system, $S/H = 34.11$ and $\frac{5H(1+N)(1/H-1)^2}{16+19N} = 6.43$. Thus, the above condition is satisfied.

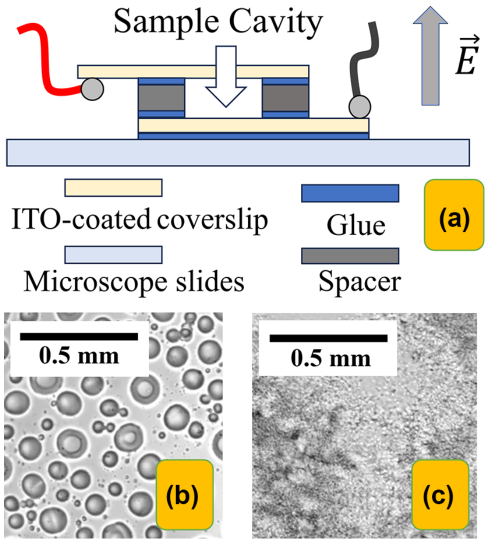

FIG. 7. Sample cell. (a) Cross-sectional schematic of a vertical-electric-field microscopy cell shows two ITO-coated coverslips separated by spacer strips, assembled on a microscope slide. This cell is used to characterize a castor oil in motor oil ([Ca:Mo]) emulsion with a low EHD threshold. (b) Coalescence-dominated regime at $E = 1\ \mathrm{V}/\mu\mathrm{m}$ (dc). (c) Droplet breakup at $E = 3.6\ \mathrm{V}/\mu\mathrm{m}$.

2. Microscopy

Electrorheology measurements were complemented by microscopy on electric field cells made from transparent cover slides coated with indium tin oxide, and with spacers to set the thickness to be $h = 270\ \mu\mathrm{m}$. Figure 7 shows the sample cell schematic for vertical-electric-field microscopy. See Sec. VI in the Supplemental Material [31] for details on the microscopy sample cells.

3. ERI preshearing

Consistent initial conditions for ERI experiments are ensured by breaking the droplets with a dc field for 10 s, followed by shearing with a linear ramp of $\bar{\dot{\gamma}}$ from 200 to $600\ \mathrm{s}^{-1}$ over 2 min. During the first minute, random pulses with different frequencies are applied to induce radial motions, ensuring a more uniform distribution of droplets in the sample. There is a 20-s period of zero shear before actual data acquisition begins. We call the whole process preshearing. Each experiment is run at least twice, with all reported values averaged between the runs.

---

[1] D. R. Link, E. Grasland-Mongrain, A. Duri, F. Sarrazin, Z. Cheng, G. Cristobal, M. Marquez, and D. A. Weitz, Electric control of droplets in microfluidic devices, Angew. Chem. Int. Ed. **45**, 2556 (2006).

[2] J. D. Wehking, L. Chew, and R. Kumar, Droplet deformation and manipulation in an electrified microfluidic channel, Appl. Phys. Lett. **103**, 054101 (2013).

[3] J. S. Eow, M. Ghadiri, A. O. Sharif, and T. J. Williams, Electrostatic enhancement of coalescence of water droplets in oil: A review of the current understanding, Chem. Eng. J. **84**, 173 (2001).

[4] S. Mhatre, V. Vivacqua, M. Ghadiri, A. Abdullah, M. Al-Marri, A. Hassanpour, B. Hewakandamby, B. Azzopardi, and B. Kermani, Electrostatic phase separation: A review, Chem. Eng. Res. Des. **96**, 177 (2015).
[5] Y. Wu and R. L. Clark, Electrohydrodynamic atomization: A versatile process for preparing materials for biomedical applications, J. Biomater. Sci. Polym. Ed. **19**, 573 (2008).
[6] R. Allan and S. Mason, Particle behavior in shear and electric fields—Deformation and burst of fluid drops, Proc. R. Soc. Lond. A Math. Phys. Sci. **267**, 45 (1962).
[7] J. Melcher and G. Taylor, Electrohydrodynamics: A review of the role of interfacial shear stresses, Annu. Rev. Fluid Mech. **1**, 111 (1969).
[8] D. Saville, Electrohydrodynamics: The Taylor-Melcher leaky dielectric model, Annu. Rev. Fluid Mech. **29**, 27 (1997).
[9] P. M. Vlahovska, Electrohydrodynamics of drops and vesicles, Annu. Rev. Fluid Mech. **51**, 305 (2019).
[10] S. Torza, R. Cox, and S. Mason, Electrohydrodynamic deformation and bursts of liquid drops, Philos. Trans. A Math. Phys. Eng. Sci. **269**, 295 (1971).
[11] E. K. Zholkovskij, J. H. Masliyah, and J. Czarnecki, An electrokinetic model of drop deformation in an electric field, J. Fluid Mech. **472**, 1 (2002).
[12] A. Varshney, S. Ghosh, S. Bhattacharya, and A. Yethiraj, Self organization of exotic oil-in-oil phases driven by tunable electrohydrodynamics, Sci. Rep. **2**, 738 (2012).
[13] S. K. Tadavani and A. Yethiraj, Tunable hydrodynamics: A field-frequency phase diagram of a non-equilibrium order-to-disorder transition, Soft Matter **13**, 7412 (2017).
[14] W. M. Winslow, Induced fibration of suspensions, J. Appl. Phys. **20**, 1137 (1949).
[15] D. G. Klingenberg, F. V. Swol, and C. F. Zukoski, Structure and dynamics of electrorheological fluids, J. Chem. Phys. **91**, 7888 (1989).
[16] Y. Z. Dong, Y. Seo, and H. J. Choi, Recent development of electro-responsive smart electrorheological fluids, Soft Matter **15**, 3473 (2019).
[17] X.-D. Pan and G. H. McKinley, Characteristics of electrorheological responses in an emulsion system, J. Colloid Interface Sci. **195**, 101 (1997).
[18] J.-W. Ha and S.-M. Yang, Rheological responses of oil-in-oil emulsions in an electric field, J. Rheol. **44**, 235 (2000).
[19] J. E. Martin and A. Snezhko, Driving self-assembly and emergent dynamics in colloidal suspensions by time-dependent magnetic fields, Rep. Prog. Phys. **76**, 126601 (2013).
[20] C. Boissy, P. Atten, and J.-N. Foulc, On a negative electrorheological effect, J. Electrost. **35**, 13 (1995).
[21] J. I. Kach, L. M. Walker, and A. S. Khair, Nonequilibrium structure formation in electrohydrodynamic emulsions, Soft Matter **19**, 9179 (2023).
[22] J. C. Baygents, N. Rivette, and H. A. Stone, Electrohydrodynamic deformation and interaction of drop pairs, J. Fluid Mech. **368**, 359 (1998).
[23] C. H. Meredith, P. G. Moerman, J. Groenewold, Y.-J. Chiu, W. K. Kegel, A. van Blaaderen, and L. D. Zarzar, Predator–prey interactions between droplets driven by non-reciprocal oil exchange, Nat. Chem. **12**, 1136 (2020).
[24] M. L. de Almeida, N. D. S. Mendes, R. M. Charin, M. Nele, and F. W. Tavares, Electro-rheological investigation on W/O emulsions morphology under electric fields, J. Dispersion Sci. Technol. **41**, 1465 (2020).
[25] B. D. Chin and O. O. Park, Rheology and microstructures of electrorheological fluids containing both dispersed particles and liquid drops in a continuous phase, J. Rheol. **44**, 397 (2000).
[26] A. Fernández, Response of an emulsion of leaky dielectric drops immersed in a simple shear flow: Drops more conductive than the suspending fluid, Phys. Fluids **20**, 043303 (2008).
[27] P. M. Vlahovska, On the rheology of a dilute emulsion in a uniform electric field, J. Fluid Mech. **670**, 481 (2011).
[28] S. Mandal, S. Sinha, A. Bandopadhyay, and S. Chakraborty, Drop deformation and emulsion rheology under the combined influence of uniform electric field and linear flow, J. Fluid Mech. **841**, 408 (2018).
[29] S. Villa, P. Edera, M. Brizioli, V. Trappe, F. Giavazzi, and R. Cerbino, Quantitative rheo-microscopy of soft matter, Front. Phys. **10**, 1013805 (2022).
[30] S. Aime, L. Ramos, J.-M. Fromental, G. Prevot, R. Jelinek, and L. Cipelletti, A stress-controlled shear cell for small-angle light scattering and microscopy, Rev. Sci. Instrum. **87**, 123907 (2016).
[31] See Supplemental Material at http://link.aps.org/supplemental/10.1103/416j-vpdj for additional experimental methods, rheology data, electroconvection, frequency dependence of EHD forces, and supporting movies.
[32] L. Marshall, C. F. Zukoski, and J. W. Goodwin, Effects of electric fields on the rheology of non-aqueous concentrated suspensions, J. Chem. Soc. Faraday Trans. 1 **85**, 2785 (1989).
[33] J. Q. Feng and T. C. Scott, A computational analysis of electrohydrodynamics of a leaky dielectric drop in an electric field, J. Fluid Mech. **311**, 289 (1996).
[34] G. K. Batchelor, The effect of Brownian motion on the bulk stress in a suspension of spherical particles, J. Fluid Mech. **83**, 97 (1977).
[35] R. R. Pethig, *Dielectrophoresis: Theory, Methodology and Biological Applications* (John Wiley & Sons, Hoboken, NJ, 2017).
[36] T. B. Jones, *Electromechanics of Particles* (Cambridge University Press, New York, 1995).
[37] K. von Pfeil, M. D. Graham, D. J. Klingenberg, and J. F. Morris, Pattern formation in flowing electrorheological fluids, Phys. Rev. Lett. **88**, 188301 (2002).
[38] J. Cao, J. Huang, and L. Zhou, Structure of electrorheological fluids under an electric field and a shear flow: Experiment and computer simulation, J. Phys. Chem. B **110**, 11635 (2006).
[39] J. S. Park and D. Saintillan, Dipolophoresis in large-scale suspensions of ideally polarizable spheres, J. Fluid Mech. **662**, 66 (2010).
[40] C. Sorgentone, J. I. Kach, A. S. Khair, L. M. Walker, and P. M. Vlahovska, Numerical and asymptotic analysis of the three-dimensional electrohydrodynamic interactions of drop pairs, J. Fluid Mech. **914**, A24 (2021).
[41] P. D. Olmsted, Perspectives on shear banding in complex fluids, Rheol. Acta **47**, 283 (2008).
[42] S. M. Fielding, Complex dynamics of shear banded flows, Soft Matter **3**, 1262 (2007).
[43] A. Montesi, A. A. Pena, and M. Pasquali, Vorticity alignment and negative normal stresses in sheared attractive emulsions, Phys. Rev. Lett. **92**, 058303 (2004).

[44] S. Caserta, M. Simeone, and S. Guido, Shear banding in biphasic liquid-liquid systems, Phys. Rev. Lett. **100**, 137801 (2008).

[45] S. Caserta and S. Guido, Vorticity banding in biphasic polymer blends, Langmuir **28**, 16254 (2012).

[46] S. Lin-Gibson, J. A. Pathak, E. H. Grulke, H. Wang, and E. K. Hobbie, Elastic flow instability in nanotube suspensions, Phys. Rev. Lett. **92**, 048302 (2004).

[47] C. O. Osuji and D. A. Weitz, Highly anisotropic vorticity aligned structures in a shear thickening attractive colloidal system, Soft Matter **4**, 1388 (2008).

[48] V. Grenard, N. Taberlet, and S. Manneville, Shear-induced structuration of confined carbon black gels: Steady-state features of vorticity-aligned flocs, Soft Matter **7**, 3920 (2011).

[49] A. S. Negi and C. O. Osuji, New insights on fumed colloidal rheology—Shear thickening and vorticity-aligned structures in flocculating dispersions, Rheol. Acta **48**, 871 (2009).

[50] A. Karppinen, T. Saarinen, J. Salmela, A. Laukkanen, M. Nuopponen, and J. Seppälä, Flocculation of microfibrillated cellulose in shear flow, Cellulose **19**, 1807 (2012).

[51] M. P. Godfrin, F. Guo, I. Chakraborty, N. Heeder, A. Shukla, A. Bose, R. H. Hurt, and A. Tripathi, Shear-directed assembly of graphene oxide in aqueous dispersions into ordered arrays, Langmuir **29**, 13162 (2013).

[52] Z. Varga, V. Grenard, S. Pecorario, N. Taberlet, V. Dolique, S. Manneville, T. Divoux, G. H. McKinley, and J. W. Swan, Hydrodynamics control shear-induced pattern formation in attractive suspensions, Proc. Natl. Acad. Sci. USA **116**, 12193 (2019).

[53] F. De Vita, M. E. Rosti, S. Caserta, and L. Brandt, Numerical simulations of vorticity banding of emulsions in shear flows, Soft Matter **16**, 2854 (2020).

[54] S. K. Tadavani, J. R. Munroe, and A. Yethiraj, The effect of confinement on the electrohydrodynamic behavior of droplets in a microfluidic oil-in-oil emulsion, Soft Matter **12**, 9246 (2016).

[55] M. Parthasarathy and D. J. Klingenberg, Electrorheology: Mechanisms and models, Mater. Sci. Eng.: R: Rep. **17**, 57 (1996).

[56] H. Ma, W. Wen, W. Y. Tam, and P. Sheng, Frequency dependent electrorheological properties: Origin and bounds, Phys. Rev. Lett. **77**, 2499 (1996).

[57] W. Y. Tam, G. H. Yi, W. Wen, H. Ma, M. M. T. Loy, and P. Sheng, New electrorheological fluid: Theory and experiment, Phys. Rev. Lett. **78**, 2987 (1997).

[58] H. J. Choi, M. S. Cho, J. W. Kim, C. A. Kim, and M. S. Jhon, A yield stress scaling function for electrorheological fluids, Appl. Phys. Lett. **78**, 3806 (2001).

[59] W. Wen, X. Huang, S. Yang, K. Lu, and P. Sheng, The giant electrorheological effect in suspensions of nanoparticles, Nat. Mater. **2**, 727 (2003).

[60] W. Wen, X. Huang, and P. Sheng, Particle size scaling of the giant electrorheological effect, Appl. Phys. Lett. **85**, 299 (2004).

[61] X. Huang, W. Wen, S. Yang, and P. Sheng, Mechanisms of the giant electrorheological effect, Solid State Commun. **139**, 581 (2006).

[62] C. Jarzynski, Diverse phenomena, common themes, Nat. Phys. **11**, 105 (2015).

[63] A. Varshney, S. Gohil, S. K. Tadavani, A. Yethiraj, S. Bhattacharya, and S. Ghosh, Large scale arrays of tunable microlenses, Lab. Chip **14**, 1330 (2014).